

Investigation of the Flow Field around a Propeller-Rudder Configuration: On-Surface Pressure Measurements and Velocity-Pressure-Phase-Locked Correlations

Mario Felli, Massimo Falchi, Francisco Pereira

CNR-INSEAN, Rome, Italy

ABSTRACT

The present paper deals with the problem of the propeller-induced perturbation on the rudder. The study aims at providing insights on the key mechanisms governing the complex interaction between the propeller wake structures and the rudder. In this regard, a wide experimental activity that concerned PIV and LDV velocity measurements and wall-pressure-measurements on the two faces of the rudder was performed in a cavitation tunnel. The major flow features that distinguish the flow field around a rudder operating in the race of a propeller were highlighted, such as the complex dynamics of the propeller tip vortices and the re-storing mechanism of the tip vortex downstream of the rudder. Wall-pressure signals were Fourier decomposed and then reconstructed, isolating the contributions of the more energetic harmonics when both the propeller phase and the rudder deflection change.

Keywords

Propeller, rudder, wall pressure, tip vortex

1 INTRODUCTION

The present trend to increase the ship speed and the propeller thrust has consequently made the problem of the mutual-interaction between the propeller and the rudder (or between the propeller and the strut in a pulling type podded propulsor) particularly critical because it is correlated directly to the hydroacoustic, structural and propulsive performance of the ship. In particular, the propeller-rudder interaction is a significant noise source that affects the acoustic signature of surface ship and the on-board comfort as the consequence of the impact and the deformation of the propeller vortex filaments, the unsteady and non-uniform inflow on the rudder and the propeller induced cavitation, mainly (Felli et al 2008).

In this scenario, the efforts towards the improvement of the ship performance requires the development of advanced numerical and experimental tools to be used for both new design approaches (as in the case of the twisted rudder (Shen et al 1997)), as well as to get a better insight into the complex mechanism of interaction with the propeller vortical structures (Felli et al 2009).

However, such an accurate analysis is a challenging task when the influence of the propeller is important and requires advanced numerical and experimental tools to resolve the complex flow around the rudder with the adequate accuracy.

On the experimental side, the problem of the propeller-rudder interaction has been widely addressed by the literature. However, most of the emphasis has been placed towards global performance (i.e., propeller and rudder loads) and cavitation measurements, as in Molland and Turnock (1992), Kracht (1992), Shen et al (1997), and Paik et al (2008), for example.

On the other hand, a few works have instead been dealing with the measure of the flow field distribution around a rudder, e.g., Felli et al (2004, 2006, 2008, 2010), Anschau & Mach (2009), and Lucke (2009).

Among these studies, the works by Felli et al (2004, 2006, 2009 and 2009a) have investigated the problem of the propeller-rudder interaction with a focus on the tip vortex/rudder interaction. These studies, performed by phase locked velocimetry measurements (i.e., LDV and PIV) and time resolved visualizations, explored different configurations of a propeller-rudder system (i.e., rudder aligned with the propeller shaft and at an offset, propeller-rudder in uniform and non-uniform inflow conditions), and has allowed highlighting some distinguishing phenomena of the tip vortex/rudder interaction as, for instance, a mechanism of breakdown of the tip vortex filaments and their recovering downstream of the rudder.

Following these works, the present paper focuses on the analysis of the interaction mechanisms between the propeller wake and the rudder, and, specifically, documents the effect of the propeller phase, the rudder deflection and the propeller inflow on the pressure field along the rudder surface. For this purpose, a special steel-rudder was manufactured to allow the detailed mapping of the pressure field along the rudder surface.

Analysis tools of the pressure data were implemented to go into the mechanisms of noise generation and to identify and characterize the perturbation sources in a propeller-rudder configuration.

In §2 and §3, we deal with the description of the experimental set up, the test matrix and the test conditions. The analysis of the results is documented in §4. In §4.1, we describe the flow field evolution around

the rudder. The distribution of the pressure field on the rudder surface is reported in §4.2. Conclusions and future works are summarized in §5.

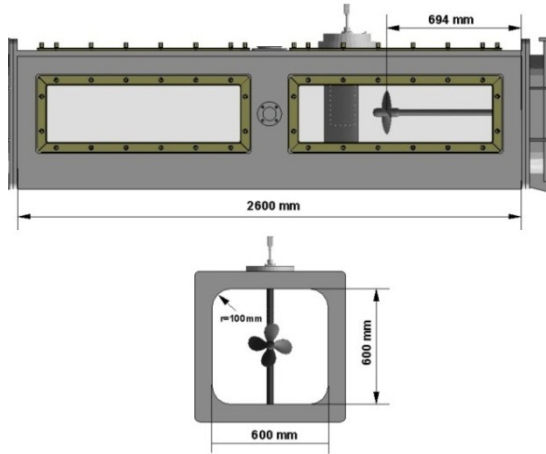


Figure 1: Propeller-rudder installation inside the tunnel.

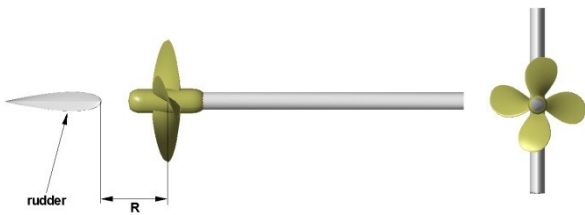


Figure 2: Propeller-rudder configuration.

2 EXPERIMENTAL SET UP

2.1 Facility and propeller-rudder configuration

Measurements were conducted in the Italian Navy Cavitation Tunnel (C.E.I.M.M.). This is a close jet tunnel with a 2.6 m long by 0.6 m span by 0.6 m deep test section. Perspex windows on the four walls enable the optical access in the test section. The nozzle contraction ratio is 5.96:1 and the maximum water speed is 12 m/s. The highest free stream turbulence intensity in the test section is 2%. In the test section, the mean velocity uniformity is within 1% for the axial component and 3% for the vertical component.

The propeller-rudder arrangement was thought to simulate the typical configuration of a single-screw ship model. Therefore, the rudder was fixed with the plane of symmetry passing through the prolongation of the propeller axis and with the leading edge at about $r=R$ from the propeller disk plane. A sketch of the experimental configuration is given in Figures 1 and 2.

Rudder geometry was simulated using an all-movable-2D-wing having a rectangular planform and standard symmetrical sections with NACA 0020 profiles. Major features of the rudder are documented in Table 1.

The model propeller was the INSEAN E779A. This propeller, object of a dataset collecting hydrodynamics and hydroacoustics measurements (Cenedese et al 1985, Stella et al 2000, Di Felice et al 2004, Pereira et al 2004, Felli et al 2009), is a four-bladed Wageningen modified

type model with a diameter of $D=227.3\text{mm}$ and a uniform pitch distribution. More detailed information on the E779A propeller is available in the aforementioned literature.

Table 1: Geometrical data of the rudder.

Rudder length	600 mm
Rudder chord	180 mm
Rudder profiles	NACA 0020
Rudder yaw axis dist. from LE	0
Rudder distance from propeller	113.5 mm

2.2 LDV experimental set up

A sketch of the LDV experimental set-up is shown at the top of Figure 3.

Flow velocity was measured by means of a two-component-back-scatter-LDV-system, which consisted of a 6W Argon Laser, a two-component underwater fiber optic probe and a 40 MHz Bragg cell for the velocity versus ambiguity removal. LDV signal processing was executed by the TSI FSA processor. In the adopted LDV system, the probe worked in backscatter and allowed measuring two orthogonal components of velocity field simultaneously. During the experiments, the probe was arranged to measure the axial and vertical components of the velocity in a fixed frame.

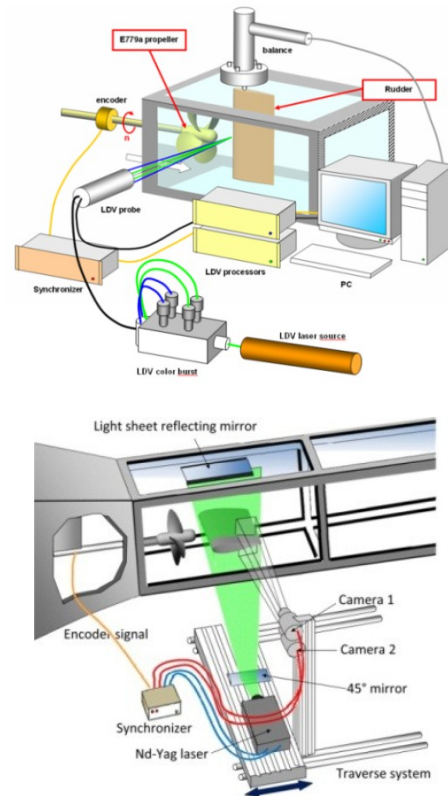


Figure 3: Experimental set up in the velocity measurements: LDV (top), PIV (bottom).

The three-dimensional velocity survey was performed in two separate steps rotating the experiment of 90°, similar to the experiment of Felli et al (2009). More specifically, two configurations with the rudder fixed on the top and side window of the test section were used to resolve the U-W and the U-V velocity components respectively.

Phase sampling techniques, i.e., Tracking Triggering Technique (TTT) (Stella et al 2000), were used to correlate the randomly acquired velocity bursts to the corresponding position of the propeller. Phase sampling of the velocity signal was carried out by a rotary 7200 pulse/revolution encoder and a synchronizer; the latter provides the digital signal of the propeller position to the TSI RMR (Rotating Machine Resolver).

The underwater probe was set up on a computer-controlled-traverse which allowed getting a displacement accuracy of 0.1mm in all the directions and to achieve a high automation of the LDV system.

Particular care was required during the initial location of the measurement volume to reduce positioning errors of the two optical configurations. This was carried out by aligning the measurement volume on a special target with known position as to the propeller disc center.

The tunnel water was seeded with 1- μ m Titanium dioxide (TiO₂) particles in order to improve the Doppler signal processor data rate.

2.3 PIV experimental set up

A sketch of the PIV experimental set up is reported at bottom of Figure 3. Rudder was mounted on the side-window of the facility, parallel to the optical axis of two CCD cameras (i.e., PCO Sencam 1028 x 1280 px²). This arrangement, with the two cameras mounted one upside the other, allowed the simultaneous imaging of the upper and lower side regions of the rudder. In this regard, the laser beam was aligned parallel to the rudder span and, then, 90-degree-rotated by a 45 deg mirror. This allowed lighting the rudder along a chordwise cross-section.

A second mirror reflecting the light sheet was placed on the top-window of the facility in order to compensate the lack of light in the regions at the leading and trailing edges of the rudder, where the curvature is such to locally block the laser sheet passage. Further details on this aspect are documented in Felli et al (2009a).

The PIV acquisition was conditioned upon the passage of the propeller reference blade for a selected angular position. This was carried out synchronizing the PIV acquisition to a TTL OPR (i.e., Once Per Revolution) signal, supplied by a signal processor fed by a 3600 pulse/sec rotary incremental encoder, mounted on the propeller dynamometer. Once triggered, the PIV synchronizer supplies a TTL signal to the two cross-correlation cameras and to a double-cavity Nd-Yag laser (200 mJ per pulse at 12.5 Hz) according to the timing diagram (150 μ sec time between pulses).

The statistical analysis was performed on a population of 500 images/phase, acquired at each propeller phase in the range 0°÷85° with the step of 5°.

Instantaneous velocity fields were acquired from a distance of 500 mm from the facility side window, using a

50 mm lens with 2.8 f-number and imaging an area of about 160 by 130 mm².

The flow field evolution was reconstructed re-assembling six different patches (i.e., three per camera), by which the whole investigation area was scanned. In this regard, the PIV system was mounted on a traverse system in order to image the different patches with the adequate precision. This operation was executed with an accuracy of 0.1 mm in order to minimize any misalignment during patch reassembling. In addition, patches were partially overlapped in order to compensate any minimal camera misalignment during the final reconstruction of the flow field evolution.

Facility water was seeded with 30-40 μ m silver coated hollow glass spherical particles with high diffraction index and density of about 1.1 g/cm³.

Image analysis was performed combining the discrete offset technique (Di Florio et al 2002) and the iterative image deformation method (Scarano & Riethmuller 2000, Scarano 2002). Prior to the analysis, the images were pre-processed subtracting the mean grey image obtained over the whole image population for a given patch and phase angle. The adopted processing set-up was composed by a 3-step discrete offset method with a final window size of 32x28 px² (i.e., interrogation windows stretched slightly in the streamwise direction) and a grid spacing between the vectors of 10 pixels (i.e., 66% overlap). The image deformation was then performed through 4 iterations with a local Gaussian weighting filter applied to the predictor field and a Gaussian sub-pixel interpolation fit.

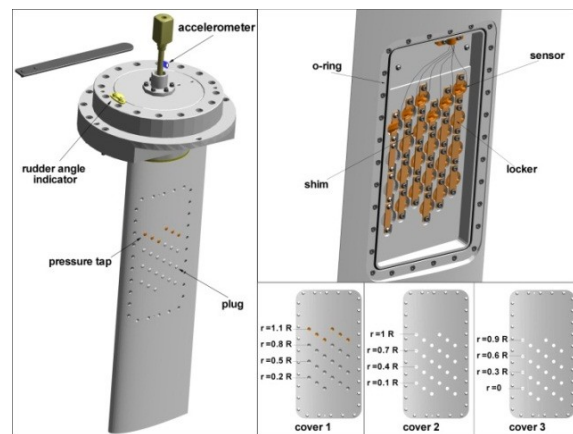


Figure 4: Sketch of the rudder instrumented for the wall-pressure measurements.

2.4 Pressure measurement experimental set up

A special steel-rudder was manufactured to allow the detailed mapping of the pressure field over the rudder surface. Specifically, pressure fluctuations were measured over a grid of 144 positions (72 positions per side), 0.1R and 0.15R spaced in the vertical and chordwise directions, respectively, and arranged to cover the region from the z=0 to z=1.1R.

A sketch of the rudder is shown in Figure 4. We flush mounted six transducers on a removable waterproof cover of the rudder, having 24 positions, arranged in four blocks with 6 positions each. All the positions in a cover were scanned moving the six transducers in the four blocks. To

improve the spatial resolution of the pressure mapping, three different series of covers were mounted on each side of the rudder. The three series had the same grid, 0.1R and 0.2R shifted each other in the vertical direction. The resulting arrangement is documented in Figure 4.

Pressure transducers were ENTRAN EPN D11 relative sensor models (i.e., 25 psi full range, 15 kHz resonant frequency, 14 mV/psi sensitivity)

Signals were acquired by a Prosig P8200 acquisition system, setting the sampling rate at 40 kHz and the acquisition time at 100 sec. Simultaneously, a once-per-revolution TTL trigger signal was acquired to synchronize the pressure signals with the angular position of the propeller reference blade. Specifically, the synchronization was carried out during the data processing on the base of the pressure signal and the propeller TTL time histories.

Then, pressure signals were phase averaged, using a slotting technique with 360 angular intervals in which pressure samples were arranged depending on the phase delay from the last trigger signal (Felli et al 2006).

3 TEST MATRIX AND CONDITIONS

Tests were carried at the free-stream velocity of $U_\infty=5$ m/s and the propeller revolution speed of $n=25$ rps, at which corresponds the advance ratio J of 0.88. Based on the rudder chord and the free-stream velocity, the nominal Reynolds number was around $Re=1.36 \cdot 10^6$. It is worth pointing out that velocities induced by the propeller give an effective Reynolds of $1.63 \cdot 10^6$.

At the testing conditions, thrust and torque coefficients on the propeller are $K_t=0.157$ and $k_q=0.0359$. These values correspond to those measured without the rudder, whose influence can be considered negligible; actually, at least for the present configuration (propeller-rudder distance $x=R$ and rudder deflection $\alpha=0$ deg).

The test matrix concerned the following activities:

- PIV measurements along 3 horizontal-chordwise and 14 vertical-chordwise sections of the wake.
- LDV measurements along 2 transversal sections of the wake just in front and behind the rudder, each having a grid of about 700 points.
- LDV measurements all along the rudder surface, Grid with 1200 positions, thickened in the tip vortex region.
- Pressure measurements all along the rudder surfaces. Grid with 144 positions (72 positions per side).

For the sake of conciseness, just some representative positions are reported hereinafter.

4 RESULT ANALYSIS

4.1 Flow field evolution

The phase locked evolutions of the axial velocity and the Y-vorticity are shown in Figures 5 and 6.

The propeller-induced cross flow makes the distribution of the flow field non-symmetrical along the opposite faces of rudder, even when the deflection angle is at zero. More specifically, in the present case (i.e., rudder with no tip aligned to the propeller shaft), the distribution of the

flow field is skew-symmetric with the pressure faces at the port side of the rotation upper region and at the starboard side of the rotation lower region.

In front of the rudder, the propeller slipstream undergoes a progressive slow down as it approaches the stagnation point. Such a deceleration causes the tip vortices and the blade trailing wake to deform progressively, as clearly documented by the iso contours of the Y vorticity in Figure 6. In particular, the tip vortices deflect outwards due to the effect of the rudder. The mechanism by which such a deflection occurs was explained in Felli et al (2009) though the model of the image vortex. The occurrence of a vorticity sheet with opposite sign to the tip vortices validates such an explanation.

During the penetration of the tip vortices into the rudder, cross-diffusion between vorticity in the boundary layer of the appendage and that within the vortex (Marshall et al 1996) causes vortex lines originating in the tip vortex to reconnect to those within the rudder boundary layer.

It results that the tip vortex is incompletely cut by the rudder: the vortex lines wrap about the leading and trailing edges and keep linked the tip vortex parts flowing on the opposite sides of the appendage. The evidence of such a complex structure is given in Figure 7: the vortex lines wrapping around the leading and trailing edges appear organized in two branches that develop close to the rudder surface on both the sides of the appendage.

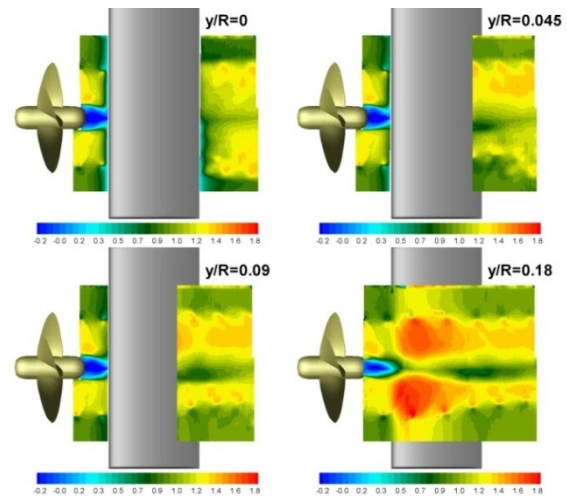


Figure 5: Phase locked PIV measurements along the longitudinal-vertical planes at $y/R=0, 0.45, 0.09, 0.18$: axial velocity.

The branch wrapping around the leading edge of the rudder stretches more and more as the tip vortex filaments are advected forward and breaks after the tip vortex leaving the trailing edge. The signature of such a progressive stretching is clearly documented in the planes at $y/R=0.09$ and $y/R=0.18$ of Figure 6.

On the other side, the vortex lines wrapping around the trailing edge keep reconnecting the tip vortex parts flowing on the face and back surfaces of the appendage downstream of the rudder, and finally restore the tip vortex (Figure 8).

The interaction with the rudder causes a spanwise displacement of the tip vortices that increases more and more chordwise. The rate of such a spanwise displacement is particularly marked for the filaments moving along the suction sides of the rudder. Instead, on the pressure side, the traces of the tip vortex describe a nearly horizontal trajectory.

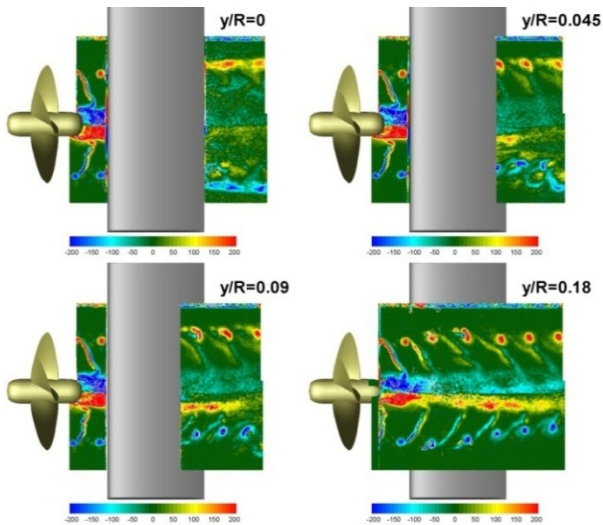


Figure 6: Phase locked PIV measurements along the longitudinal-vertical planes at $y/R=0, 0.45, 0.09, 0.18$: Y-vorticity.

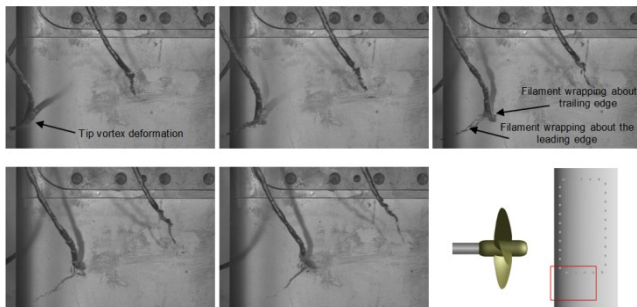


Figure 7: Tip vortex destabilization while penetrating the rudder: note the cavitating branches that develop close to the rudder surface. Snapshots are here spaced 0.0075 sec.

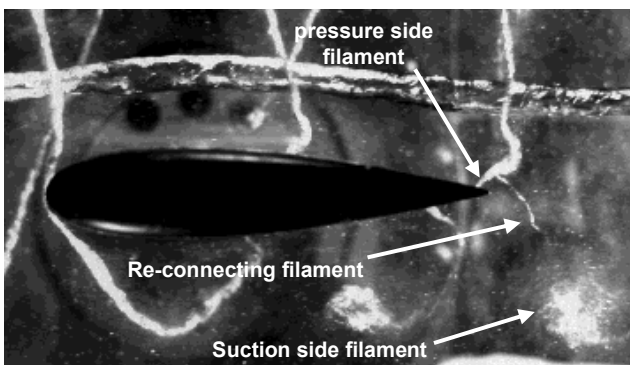


Figure 8: Visualization of the tip-vortex re-joining mechanism (courtesy of Felli et al (2009)).

The features of such a spanwise misalignment are the result of the combined effect of the spanwise gradient of the pressure distribution and the image vortex, according to what documented in Figure 9. More specifically:

- i) In both the rotation upper and lower regions, the larger dynamic pressure in the propeller wake makes the distribution of the pressure field increasing outwards moving spanwise from the radial position where propeller develops maximum thrust (i.e., $r=0.7R$) (see picture at top-right of Figure 9 which shows the distribution of the total pressure on the rudder surface). Therefore, the corresponding spanwise gradient of the pressure field is inward oriented locally, as represented by the yellow arrow in Figure 9.
- ii) The effect of the image vortex is such to displace upward (downward) the tip vortices in the port side (starboard side) of the rudder when the propeller is rotating clockwise, as explained in Felli et al (2006).

According to the observations in i) and ii), the convective motion induced by the image vortex occurs with a favorable (adverse) pressure gradient in the suction (pressure) side of the rudder, and, thus, results in a larger (smaller) displacement. It follows that such a different trend results in a continuously larger spanwise deviation between corresponding tip vortex filaments which attains its maximum at the trailing edge of the rudder.

From about mid-chord of the rudder, the tip vortex branches wrapping around the trailing edge start to describe a spiral geometry whose radius becomes bigger and bigger streamwise. The spiral appears rolling up in the opposite direction to the filament rotation and, specifically: clockwise (counterclockwise) for the filament on the pressure (suction) side of the rudder.

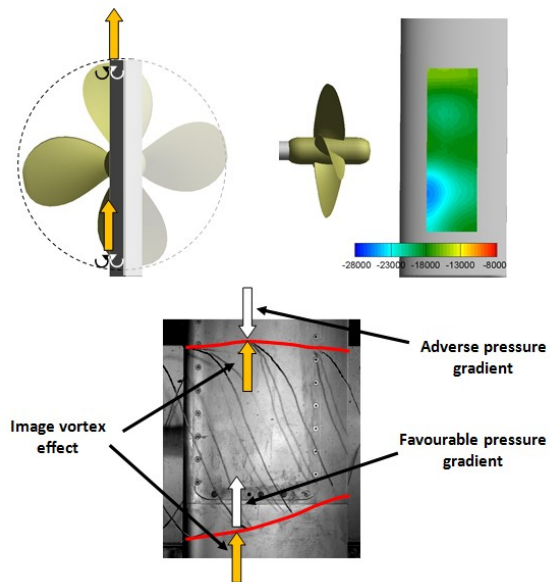


Figure 9: Explanation of the different spanwise displacement of the pressure and suction side filaments: effect of the image vortex (top-left), pressure distribution along the rudder surface (top-right), effect of the image vortex and the pressure gradient on the trajectories of the pressure and suction side filaments (bottom).

The signature of the aforesaid roll up is also captured in the contour plots of the Y-vorticity, as clearly documented in the planes at $y/R=0.09$ and $y/R=0.18$ of Figure 6. Here, the spiraling geometry of the vortex filament is resolved as a vorticity core (clockwise rotating in the pressure side) surrounded by a counter-rotating vorticity sheet which suddenly appear at about the mid-chord region of the rudder: the former is induced by the roll up of the spiral, the latter concerns the vorticity of the vortex filament.

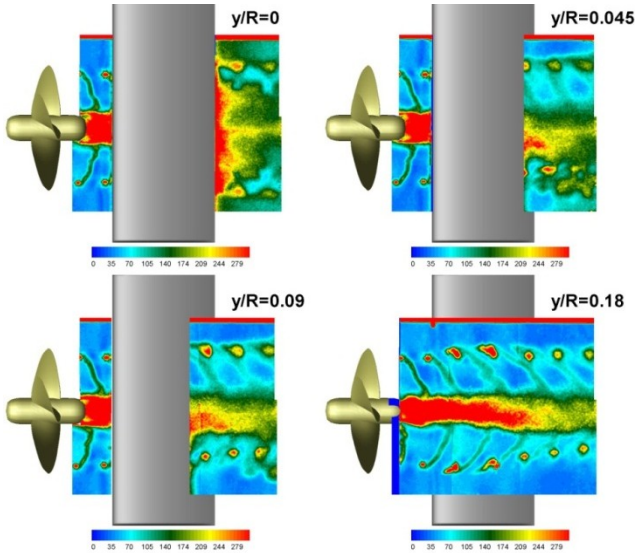


Figure 10: Phase locked PIV measurements along the longitudinal-vertical planes at $y/R=0, 0.45, 0.09, 0.18$: Y-vorticity fluctuations.

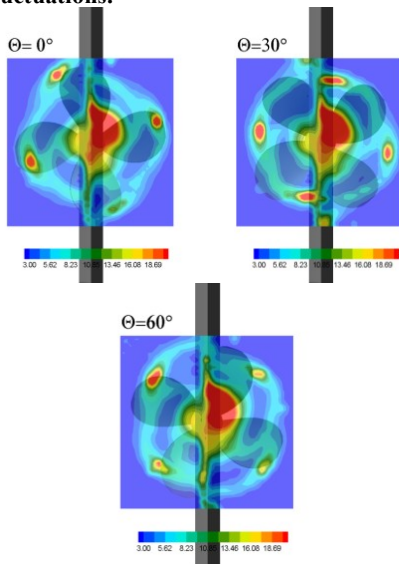


Figure 11: Phase locked LDV measurements along the transversal planes just behind the rudder: turbulent kinetic energy at $\theta=0^\circ, \theta=30^\circ$ and $\theta=60^\circ$.

The distribution of the vorticity fluctuations measured by PIV is documented in Figure 10. Figure 11 shows the distribution of the turbulent kinetic energy as measured by LDV along the transversal plane just behind the rudder. More specifically, the following considerations

are worth being outlined from the analysis of Figures 10 and 11:

- The vorticity fluctuations are correspondently maximum to the traces of the propeller structures (i.e., tip and hub vortices, blade wake trailing vorticity) and all along the trailing wake of the rudder.
- The intensities of the vorticity fluctuations in the trailing wake of the rudder are very strong just behind the trailing edge of the appendage and, then, they reduce rapidly streamwise. In addition, the streamwise decay of the vorticity fluctuations occurs with a smaller and smaller extent of the turbulent trace of the trailing wake vorticity, both along the streamwise and the transversal directions: this seems to suggest that viscous dissipation has prevalence over turbulent diffusion effect in the boundary layer eddies of the rudder.
- The marked turbulent nature of the tip vortex re-joining mechanism is clearly documented in contour plots at $y/R=0.45$ and $y/R=0.9$ of Figure 10. The traces of the re-joining face and back filaments of the tip vortex are clearly recognizable in the rotation lower side, whereas no evidence of the re-joining process is noticed on the rotation upper side. This different behavior is given considering that the re-joining process does not occur along the symmetry plane of the rudder but it is shifted towards the direction along which the tip vortex moves.
- The levels of turbulence in the hub vortex are not homogeneously distributed transversally and show maximum values on the starboard side region, as shown in Figure 11.

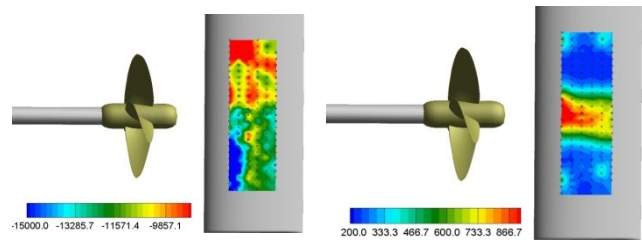


Figure 12: Phase locked mean (top) and root mean square (bottom) values of the pressure signals.

4.1 Pressure field

Pressure signals on the rudder surface were sampled M times during each propeller revolution and then, ensemble averaged according to the following relation:

$$\langle p \rangle_i = \frac{1}{N} \sum_{j=1}^N p_{i,j} \quad (1)$$

in which j and i are the corresponding j -th revolution and the i -th data point in that revolution and N the propeller revolutions performed during each acquisition.

The ergodicity of the random process involved, allows the average pressure-time history obtained from Eq. (1) to be transposed into the frequency domain by the Direct Fourier Transform.

In mathematical terms, the Fourier's theorem asserts that, for a periodic function $p(t)$ of fundamental frequency f_0 ,

one can write p as the sum of basic trigonometric functions such that:

$$p(t) = \sum_{n=0}^{\infty} A_n \cos(2\pi n f_0 t + \varphi_n) \quad (2)$$

in which A_n and φ_n represent the amplitude and phase of the corresponding harmonic function.

Equation (2) can be rearranged into:

$$p(t) = \sum_{n=0}^{\infty} C_n \cos(2\pi n f_0 t) + \sum_{n=0}^{\infty} S_n \sin(2\pi n f_0 t) \quad (3)$$

The determination of A_n and φ_n in (1) is now reduced to the calculation of the coefficients C_n and S_n , using the following formulas:

$$C_0 = f_0 \int_{-f_0/2}^{f_0/2} p(t) dt$$

$$C_m = 2f_0 \int_{-f_0/2}^{f_0/2} p(t) \cos(2\pi m f_0 t) dt \quad m \neq 0 \quad (4)$$

$$S_m = 2f_0 \int_{-f_0/2}^{f_0/2} p(t) \sin(2\pi m f_0 t) dt$$

The above transform decomposes a periodically unsteady signal into its basic components, i.e., the fundamental frequency or first harmonic, and its multiples or higher order harmonics, and, thus, allows sorting out the phase-locked coherent flow structures from the otherwise random unsteadiness in the flow field.

In the present work, the fundamental frequency is associated to the blade passage, which corresponds to the rotation speed times the number of blades. More specifically, the blade passage frequency (BPF) is here equal to 100 Hz, the propeller rotation speed being 25 rps and the number of blades 4.

The statistical analysis is calculated over the 2500 propeller revolutions performed during the 100s of measurement.

The harmonic decomposition is an extremely useful tool by which one can reconstruct the phase-locked topologies of each single harmonic in the measurements domain, and, consequently, isolate the corresponding perturbation sources (e.g., correlating the phase-locked representation of each harmonic to corresponding representations of the velocity signals or visualizations).

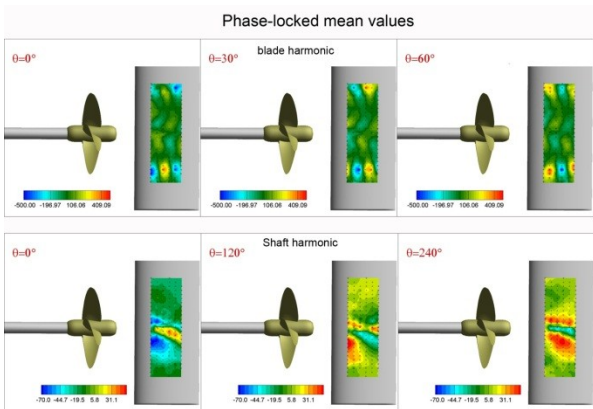


Figure 13: Pressure measurements on the rudder. Evolution of the phase averaged pressure signal reconstructed using only the blade harmonic (top) and the shaft harmonic (bottom).

The distribution of the phase-locked pressure field along the rudder gives a quantitative estimation of the pressure levels on the pressure (top) and suction (bottom) side regions of the appendage. Specifically, the following considerations can be made with reference to Figure 12:

- The effect of the propeller perturbation makes markedly different the pressure levels on the upper and lower side regions of the rudder. Such a difference is estimated to be around 2000 Pa on average.
- On the suction side, a low pressure region occurs at about 30% of the chord. More downstream the pressure values increase quite suddenly and reach the maximum at about mid-chord.
- The traces of the tip vortex filaments and the hub vortex are clearly isolated in the contour plot of the wall-pressure fluctuations. In particular, the maximum values of the fluctuations are observed in the hub vortex at nearly the leading edge region. More downstream, starting from about 25% of the chord, the intensity of such fluctuations tends to reduce more and more.

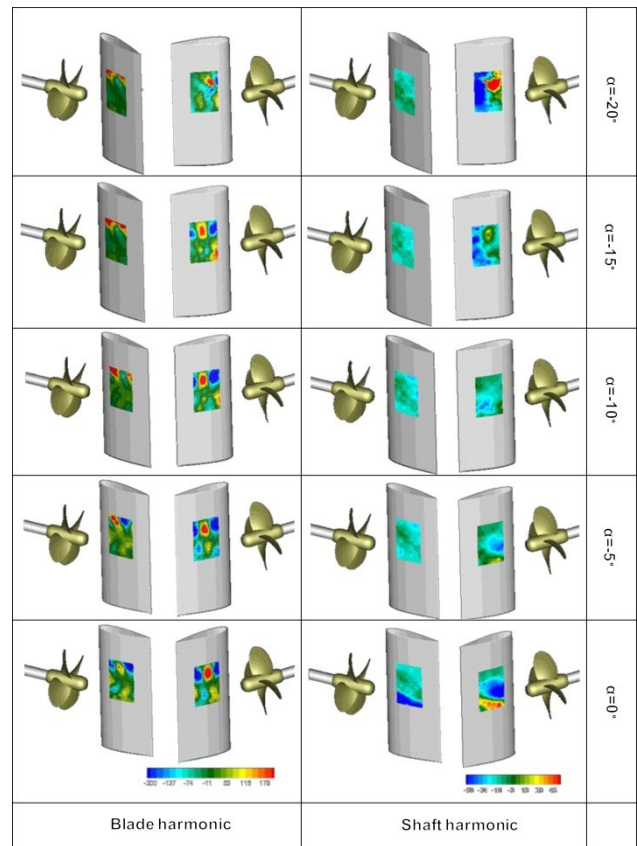


Figure 14: Phase locked evolution of the blade and shaft harmonics of the pressure field against rudder deflection (color scale is related to all graphs).

The phase locked evolution of the shaft and blade harmonics is described in the contour plots of Figure 13, for three different angular positions of the propeller, at zero deflection.

During a propeller rotation, the mean values of the shaft harmonic exhibit the larger fluctuations in the rotation lower side of the propeller and correspondingly to the hub vortex region. A different behavior is, instead, observed

in the contour plots of the blade harmonic that fluctuate periodically attaining the maximum values of the peak-to-peak distance in correspondence of the tip vortex region.

The intensities of such fluctuations are estimated to be around 1% of the original signal for the shaft harmonic and around 10% for the blade harmonic.

The intensity and the topology of the shaft and blade harmonics are differently influenced by the deflection angle of the rudder, as highlighted in the iso-contours of Figure 14. The traces of the tip vortices and the blade trailing wakes stand out from the iso-contours of the blade harmonic. The intensities of these perturbations are maximum when the rudder deflection is set at zero. The intensity of the pressure fluctuations in the tip vortex does not experience a significant reduction when the deflection angle is kept increasing, at least until $\alpha=-15^\circ$. When the deflection angle changes, the different position of the rudder as to the incoming propeller wake causes a phase displacement in the induced pressure perturbation.

The topology and the intensity of the perturbation at the shaft harmonic show a strong correlation to the deflection angle of the rudder. For α ranging from -10° to 0° , the largest fluctuations are observed in the low pressure face of the rudder, with peaks localized correspondently to the region under the influence of the hub vortex, as previously mentioned. For values of the deflection angle larger than 10° , the afore-described topology of the component at the shaft harmonic undergoes a dramatic change. Our concern is that the explanation for such an abrupt change has to be found in the effect of the deflection angle against the geometry of the hub vortex. The analysis of the animation supports this conjecture:

- For rudder deflections less than a critical value, both the faces of the rudder suffer the hub vortex associated perturbation, more or less likewise.
- Just over such a critical value (here estimable between 10° and 15°), the rudder surface in the shadow of the propeller wake is definitively screened from the hub perturbation.

In the contour plot at $\alpha=-20^\circ$ of Figure 14, the sudden disappearance of any perturbation in phase with the propeller from about mid-chord of the suction face of the rudder (iso-contours of the starboard face of the rudder in Figure 14) is indicative of a stall condition.

5 CONCLUSIONS AND FUTURE WORKS

The present paper deals with the problem of the propeller-rudder interaction and it focuses on the analysis of the evolution mechanisms of the propeller vortical structures under the interference of the rudder.

The study concerned a wide experimental activity in which PIV and LDV velocity measurements, rudder-surface-pressure measurements and time resolved visualizations were used to investigate the flow field around a propeller-rudder configuration operating in open water.

Collected data allowed describing major flow features that distinguish the interaction of the propeller tip and hub vortices with the rudder, with special emphasis to the unsteady-flow aspects. Specifically:

- The propeller tip vortices undergoes a progressive deformation and a spanwise outwards displacement when approaching the leading edge of the rudder. During the interaction with the rudder the tip vortex splits in two branches which flow on the opposite sides of the appendage, kept linked by vortex lines embedded in the boundary.
- A different rate of the spanwise displacement is observed in the tip vortex filaments running on the pressure and suction sides of the rudder. This difference is the consequence of the convective motion induced by the image vortex that occurs with a favorable (adverse) pressure gradient in the suction (pressure) side of the rudder.
- Downstream of the rudder the vortex lines wrapping around the trailing edge make reconnecting the tip vortex parts flowing on the face and back surfaces of the appendage, restoring the tip vortex.

Pressure signals on the rudder surfaces were Fourier decomposed and then reconstructed isolating the contributions of the most energetic harmonics. This approach was proved to be an effective tool for the identification of the perturbation sources affecting the propeller-rudder interaction.

The analysis of the instantaneous pressure and velocity signals is considered a suitable tool to further investigate into the complex dynamics of the tip vortex filaments. In this regard advanced methodologies for signal analysis based on the application of advanced time-frequency signal decomposition techniques, as the wavelet transforms, and other more standard methods commonly used for reduced order modeling, such as the Linear Stochastic Estimation (LSE) and the Proper Orthogonal Decomposition (POD) are going to be used for a more in-depth analysis of the instability and breakdown mechanisms.

Moreover, the marked unsteady and three dimensional nature of the flow field suggests integrating the analysis with Stereo-PIV and time resolved PIV measurements.

The present data are going to be made available for downloading by request to the authors.

ACKNOWLEDGMENTS

This work was supported by the Italian Ministry of Defense in the framework of the research project "PRIAMO".

REFERENCES

- Anscha, P. & Mach, K.P. (2009) 'Stereoscopic PIV measurements of rudder flow and vortex systems in the towing task'. *ATM 09*, Nantes, France.
- Di Florio, G., Di Felice, F. & Romano, G. P. (2002). 'Windowing, re-shaping and reorientation interrogation windows in particle image velocimetry for the investigation of shear flows'. *Measurement Sci. Technol.* 13, pp. 953-962.
- Felli, M., Camussi, R. & Guj, G. (2009). 'Experimental analysis of the flow field around a propeller-rudder configuration'. *Experiments in Fluids* 46.

- Felli, M. & Di Felice, F. (2004). 'Analysis of the propeller-hull interaction by LDV phase sampling techniques'. Journal of Visualization **7**(1).
- Felli, M. & Di Felice, F. (2005). 'Propeller wake analysis in non-uniform inflow by LDV phase sampling techniques'. Journal of Marine Science and Technology **10**(4), pp. 159-172.
- Felli, M., Di Felice, F., Guj, G. & Camussi, R. (2006). 'Analysis of the propeller wake evolution by pressure and velocity phase measurements'. Experiments in Fluids **1**, pp. 1-11.
- Felli, M., Falchi, M. & Di Felice, F. (2009a). 'PIV analysis of the mechanism of evolution and interaction of the propeller tip vortices with a rudder'. 8th International Symposium on Particle Image Velocimetry, Melbourne, Australia.
- Felli, M., Greco, L., Colombo, C., Salvatore, F., Di Felice, F. & Soave M. (2006). 'Experimental and theoretical investigation of propeller-rudder interaction phenomena'. 26th Symposium on Naval Hydrodynamics, Rome, Italy.
- Huang, H. T., Fielder, H. F. & Wang, J. J. (1993). 'Limitation and improvement of PIV; part II: Particle Image Distortion, a novel technique'. Exp. Fluids **15**, pp. 263-273.
- Kracht, A. M. (1992). 'Ship propeller rudder interaction'. 2nd International Symposium on Propeller and Cavitation, Hangzhou, China.
- Lücke T. & Streckwall H. (2009). 'Cavitation Research on a Very Large Semi Spade Rudder'. First International Symposium on Marine Propulsors, SMP'09, Trondheim, Norway.
- Marshall, J. S. & Grant, J. R. (1996). 'Penetration of a Blade into a Vortex Core: Vorticity response and Unsteady Blade Forces'. Journal of Fluid Mechanics **306**, pp. 83-109.
- Molland, A. F. & Turnock, S. R. (1992). 'Wind tunnel investigation of the influence of propeller loading on ship rudder performance'. The Royal Institution of naval Architects, London, UK.
- Paik, B. G., Kim, K. Y., Ahn, J. W., Kim, Y. S., Kim, S. P. & Park, J. J. (2008). 'Experimental study on the gap entrance profile affecting rudder gap cavitation'. Ocean Engineering **35**, pp. 139-149.
- Scarano, F. (2002). 'Iterative image deformation methods in PIV'. Measurement. Sci. Technol. **13**, pp. 1-19.
- Shen, Y. T., Jiang, C. W. & Remmers, K. D. (1997). 'Effect of ship hull and propeller on rudder cavitation'. Journal of Ship Research, pp. 41-44.
- Shen, Y. T., Remmers, K. D. & Jiang, C. W. (1997). 'Effect of ship hull and propeller on rudder cavitation'. Journal of Ship Research, pp. 41-43.